Nanoscale

PAPER

View Article Online
View Journal | View Issue

Cite this: *Nanoscale*, 2015, **7**, 14760

A vertical-oriented WS_2 nanosheet sensitized by graphene: an advanced electrocatalyst for hydrogen evolution reaction†

Tofik Ahmed Shifa,‡[a,b] Fengmei Wang,‡[a,b] Zhongzhou Cheng,[a] Xueying Zhan,[a] Zhenxing Wang,[a] Kaili Liu,[a,b] Muhammad Safdar,[a] Lianfeng Sun*[a] and Jun He*[a]

Received 5th June 2015,
Accepted 3rd August 2015

DOI: 10.1039/c5nr03704b

www.rsc.org/nanoscale

Electrocatalytic hydrogen production at low overpotential is a promising route towards a clean and sustainable energy. Layered transition metal dichalcogenides (LTMDs) have attracted copious attention for their outstanding activities in hydrogen evolution reaction (HER). However, the horizontally laid nanosheets suffer from a paucity of active edge sites. Herein, we report the successful synthesis of vertical-oriented WS_2 nanosheets through a hydrothermal method followed by a facile sulfurization process. Furthermore, the surface of synthesized WS_2 nanosheets was decorated by ultrathin reduced graphene oxide (rGO) nanoplates. This is achieved for the first time by bringing the rGO on the surface of vertical-oriented WS_2 nanosheets, which is conducive to rapid electron transport during the HER process. Significantly, the as-synthesized rGO/WS_2 nanosheets exhibit improved HER activity as compared to the undecorated ones. It needs a low overpotential of only 229 mV *vs.* RHE to afford a current density of 10 mA cm^{-2}. We believe that this hybrid structure demonstrated remarkable HER activity brought about by a compatible synergism between rGO and WS_2.

Introduction

The ever-increasing energy consumption continues to be the world's main concern. At some point in the near future, the global community undoubtedly will depend on the greenest method of powering our world not only for environmental remedies, but also for scarcity due to oil crisis.[1] Thus, there is an urgent need for renewable and environmentally sustainable energy technologies. In this respect, hydrogen economy is a promising route[2] as the combustion of hydrogen fuel gives just pure water. However, the production of H_2 from water is thermodynamically an uphill process. Specifically, electrocatalytic production of hydrogen from water requires high overpotential. To lower the overpotential, thereby improving the energy efficiency, research studies are taking place to design a good hydrogen evolution reaction (HER) catalyst. The platinum metal is the best catalyst under acidic or neutral conditions, being highly active and producing a high current density at a very low overpotential of ~0 V *vs.* RHE. But it is scarce and expensive, which could be unaffordable for scalable applications.[3–6] Great efforts have, therefore, been devoted to the exploration of earth-abundant materials. In such a quest, experiments and theoretical calculations suggest that the layered transition metal dichalcogenide (LTMD) materials, such as MoS_2, are good prospects to replace Pt for electrochemical hydrogen evolution.[7–11] It has been proved that their promising electrocatalytic properties are brought about mainly by their exposed edge sites.[12–14]

WS_2, as one kind of LTMD, finds numerous applications in fluorescent emitters,[15] field effect transistors[16], photovoltaics[17], photocatalysis[18], energy storage[19] and electrocatalysis.[3,4,20,21] To date, the growth techniques for WS_2 nanosheets are focused to maximally expose the active edge sites. In this regard, exfoliation[3,21] is a commonly known technique. It allows for the preparation of large amounts of monolayers. However, apart from resulting in polydispersed distribution of flakes, it also suffers from the difficulty of lack of control over the size, shape or nature of their edges.[21,22] Notably, despite elimination of the laborious electrode preparation steps, it has been observed that growth on a suitable substrate creates large monolayers with high crystallinity and ease of control over shapes and edges.[23] So far the growth of WS_2 nanosheets

[a]*CAS Key Laboratory of Nanosystem and Hierarchical Fabrication, National Center for Nanoscience and Technology, No. 11 ZhongGuanCunBeiYiTiao, 100190 Beijing, P.R. China. E-mail: hej@nanoctr.cn, slf@nanoctr.cn*

[b]*University of Chinese Academy of Science, No. 19A Yuquan Road, Beijing 100049, China*

†Electronic supplementary information (ESI) available: The SEM image of rGO/WS_2 (Fig. S1), XRD patterns of WS_2 (Fig. S2), Raman spectra of WS_2 (Fig. S3), and voltammograms at various scan rates for C_{dl} estimation (Fig. S4). See DOI: 10.1039/c5nr03704b

‡These authors contributed equally to this work.

reported has been in line with the substrate. Such horizontally laid nanosheets experience a paucity of active edge sites, as part of their sides remains unexposed. On the contrary, the vertical alignment has the benefit of exposing the maximum active edge sites, availing more surface area for electrocatalytic activity and most importantly, it will form an intimate hybrid structure like WS_2–rGO. The design of the hybrid heterostructure has immense application in catalysis for its synergetic effect.[24–28] Particularly, the heterostructures made with rGO amplify the electrocatalytic activity because of their excellent properties, such as good conductivity, chemical durability and large surface area.[29,30] As a matter of fact, the vertical alignment of WS_2 nanosheets will have a more appropriate orientation to form a well-matched hybrid. Moreover, the computational study has confirmed that graphene can be adsorbed onto the surface of the WS_2 monolayer[31] due to the nearly linear band dispersion relationship of graphene that can be preserved in the rGO/WS_2 hybrid system. It is thus expected that sensitization of vertically oriented WS_2 nanosheets by rGO will enhance the electrocatalytic activity toward HER.

Herein, we, for the first time, report the successful design of the synthesis of vertically aligned WS_2 nanosheets through sulfurizing WO_3 nanotrees on the W foil. The branches on the nanotrees led to the *in situ* formation of vertically oriented WS_2 nanosheets directly. Moreover, we further decorated the vertically positioned WS_2 nanosheets by rGO. The comparison was also made between rGO decorated and undecorated WS_2 nanosheets. Accordingly, the obtained electrodes achieved a remarkable current density of 10 mA cm^{-2} at 229 mV and 236 mV *vs.* RHE in the case of rGO/WS_2 and WS_2 respectively. Significantly, a smaller Tafel slope was recorded for rGO/WS_2 (73 mV dec^{-1}) as compared to the bare WS_2 (97 mV dec^{-1}). We believe that the well-established synergism between rGO and WS_2 played a significant role which brought about rapid electron transport leading to the enhanced HER activity.

Experimental

Synthesis of a WO_3 nanotree

The hydrothermal method was employed to synthesize the WO_3 nanotree.[32] Typically, the W foil was cleaned ultrasonically in distilled water, ethanol, and acetone and then dried by N_2 gas. The cleaned W foil was annealed in air at 500 °C for 30 min. The oxidized tungsten metal plate was placed in an autoclave with an aqueous solution containing $H_2C_2O_4$ (1.56 g), Rb_2SO_4 (0.2 g), and concentrated HNO_3 (313 μL), and treated at 150 °C for 72 h. After the hydrothermal reaction, the foil was washed with deionized water and dried at room temperature. This sample was then annealed in air at 500 °C for 30 min to reduce oxygen defects in WO_3.

Synthesis of WS_2 nanosheets and sensitization

The as-prepared WO_3 nanotree was placed at the back zone of the quartz tube in the furnace, whereby the S powder was located at the front zone. With such an arrangement, the tube was flushed with Ar gas three times and pumped into a vacuum lower than 1 Pa. The back zone was raised to 800 °C at a heating rate of 20 °C min^{-1}, the front zone began to increase in temperature to 150 °C at a rate of 10 °C min^{-1}. The conversion process was maintained for 60 min with 50 sccm Ar gas flow. After the conversion process, the furnace was allowed to cool to room temperature. The as-grown WS_2 sample was then soaked in reduced graphene oxide. The rGO was first prepared by reduction of GO[33] by treating it with hydrazine.[34]

Characterization and electrochemical measurement

A field emission scanning electron microscope (FESEM, Hitachi S-4800), a transmission electron microscope (TEM, Tecnai F20), a confocal microscope-based Raman spectrometer (Renishaw InVia, 532 nm excitation laser), X-ray diffractometer (Philips X'Pert Pro Super with Cu Kα radiation) and a X-ray photoelectron spectrometer (ESCALAB250Xi) were used to characterize the sample. Electrochemical measurements were carried out with a 3-electrode cell using an electrochemical station (CHI 660D, 0.5 M H_2SO_4 electrolyte with Pt as a counter electrode, SCE as a reference electrode and the material under investigation as a working electrode, at a scan rate of 2 mV s^{-1}). The system was continuously de-aerated with N_2. Linear sweep voltammogram was measured; all the measured potentials were calibrated with respect to RHE. To determine the electrochemical active surface area, a cyclic voltammeter at various scan rates (20–200 mV s^{-1}) was run in the potential range of −0.1 V to 0.0 V *vs.* RHE. Alternating current impedance measurements were performed in the same configuration in the frequency range from 0.01 Hz to 0.5 MHz with an AC voltage of −0.1 V *vs.* RHE.

Results and discussion

Visually, Fig. 1 depicts the schematic representation of our experimental steps. Following the hydrothermal synthesis of WO_3 nanotrees,[32] it was subjected to sulfurization. Sulfur powder was made to flow through the two zone tube furnace by Ar gas flow to keep the growth zone saturated by sulfur. At the growth zone, the WO_3 nanotree on the W foil substrate was

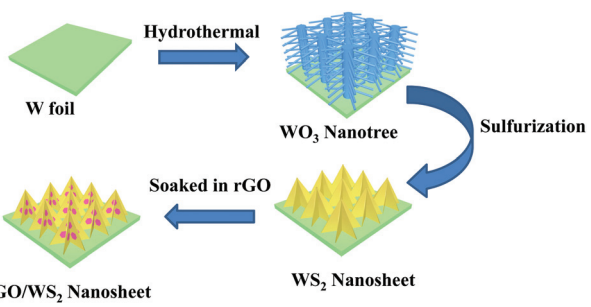

Fig. 1 Schematic showing the experimental steps of synthesizing the WO_3 nanotree, WS_2 nanosheet and rGO/WS_2 nanosheet on the W foil.

heated at 800 °C, and thereby sulfurized completely. The converted WS_2 was sensitized by rGO to be used in HER (see the Experimental section).The morphology and structure of the as-synthesized samples were first characterized by scanning electron microscopy (SEM) and transmission electron microscopy (TEM). Fig. 2a–c show the SEM images of WO_3, WS_2 and rGO/WS_2. It can be seen that the tungsten foil is entirely covered by WO_3 nanotrees, growing vertically to the substrate, composed of a great deal of trunks and branches. The average diameter and length of the trunks in the nanotree are estimated to be 57 ± 8 nm and 0.78 ± 0.14 μm respectively; whereas those of the branches are 29 ± 3 nm and 0.19 ± 0.075 μm respectively. As reported,[35] different cations of sulfate play a significant role in shaping the morphology; and Rb^+ leads to the formation of the nanotree.[36] The W foil substrate served as the self-seeded substrate on which the WO_3 layer grew. Pre-annealing of the W foil led to the adhesion between WO_3 and the substrate. Thus, the dense oxidative layer formed at the beginning of the hydrothermal treatment became the nuclei for the subsequent growth of the WO_3 nanotree. The branches of the nanotree show a tendency to become nanosheets, where on sulfurization, the entire morphology changes to nanosheets with thickness of about 27.8 ± 6 nm (the inset of Fig. S1d†). Interestingly, the vertical alignment remained unaffected. The sulfurization takes place under an Ar atmosphere in a horizontal tube furnace at 800 °C. The as-synthesized WO_3 nanotree is converted to WS_2 nanosheets by sulphur vapour as:

$$7S + 2WO_3 \rightarrow 2WS_2 + 3SO_2$$

Sulfur has a considerably larger atomic radius compared to oxygen, which can induce structural distortion, and hence changes in morphology when S atoms substitute oxygen in the WO_3 lattice. However, there is no change in morphology of WS_2 after sensitization with rGO can be seen from Fig. 2c (also in Fig. S1d†). It is obvious that the surface of WS_2 nanosheets is decorated by rGO and the composition of rGO is estimated to be about 2.83% from thermogravimetric analysis (Fig. S5†).

We further verified the presence of rGO by the characteristic D and G bands from the Raman spectrum and the elemental composition from X-ray photoelectron spectroscopy (XPS). To confirm the presence and ratio of S atoms, elemental composition analysis was performed by energy dispersive X-ray (EDX). Fig. 2d reveals the EDX spectrum of the as-prepared WS_2 material. A W/S ratio of approximately 1 : 2 is obtained which is consistent with the expected one. The HRTEM image (Fig. 2e–f) shows a stacking morphology of hexagonally arranged atoms of crystalline WS_2 nanosheets. Moreover, the periodic arrays of (101) planes with a spacing of 0.27 nm can clearly be observed. This is also in accordance with the peak obtained at the 2θ value of 32.93° from the X-ray diffraction (XRD) spectrum. The XRD pattern of rGO/WS_2 hybrid nanosheets is shown in Fig. 3a. The reflections at 14.29, 32.93, 58.18 corresponding to (002), (101), and (110) planes indicate the presence of the hexagonal phase (PDF# 084-1398). This indicates successful conversion to the corresponding sulfide as the characteristic XRD peaks (Fig. S2†) corresponding to WO_3 diminished due to sulfurization. Some slight shift of the peak position and broadening can also be observed for rGO/WS_2 as compared to pristine WS_2 (Fig. S3†). The increased peak broadening indicates the formation of a thin-layer of nanosheets.

To further investigate the constituents of the as-synthesized nanosheets, composition-dependent vibration modes were obtained from the Raman spectrum. Accordingly, the Raman spectrum in Fig. 3b illustrates the characteristic peaks of WO_3, WS_2 and rGO. The peaks revealing O–W–O vibrations in WO_3[37] diminished upon sulfurization, and a new feature was introduced in WS_2. The prominent first-order Raman-active modes for WS_2 corresponding to E_{2g}^1 and A_g^1 can be identified at 350 cm^{-1} and 419 cm^{-1} respectively; the small peak at 345 cm^{-1} is attributed to the 2LA mode.[38,39] The bands at 1349 cm^{-1} and 1604 cm^{-1} are meant for the D and G bands of rGO. These are not present in the Raman spectra of pristine WS_2 (Fig. S3†), which confirms that the surface of WS_2 is modified by rGO. The rest of the bands (583 cm^{-1}, 705 cm^{-1})

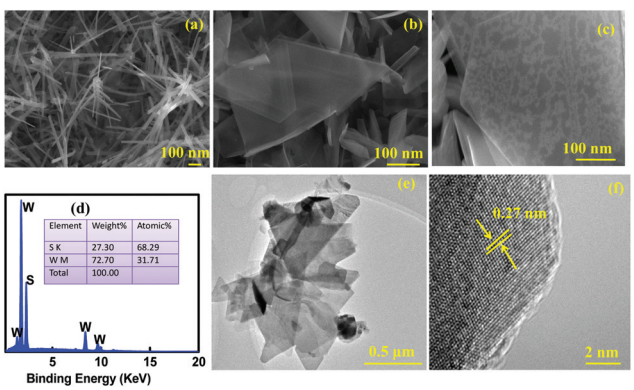

Fig. 2 SEM image of (a) WO_3, (b) WS_2, (c) rGO/WS_2, (d) EDX result for elemental WS_2, (e) TEM image of rGO/WS_2, and (f) HRTEM image of rGO/WS_2.

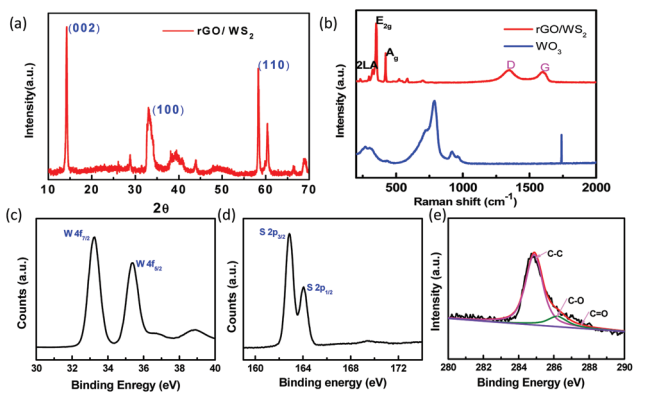

Fig. 3 (a) XRD pattern, (b) Raman spectra of rGO/WS_2, (c–e) XPS spectra of W 4f, S 2p and C 1s in rGO/WS_2 respectively.

can be assigned to a combination of the sum and differences of individual phonon modes of vibrations (A_g^1(M) + LA(M), 4LA(M)).[38] X-ray photoelectron spectrometry (XPS) was employed to identify the elemental states of rGO/WS_2. In Fig. 3c, the characteristic W^{4+} oxidation state can be associated with the peaks observed at 33.2 and 35.4 eV which are attributed to W $4f_{7/2}$ and W $4f_{5/2}$. The peaks at 162.8 and 164 eV in Fig. 3d are meant for S $2p_{3/2}$ and S $2p_{1/2}$, respectively. Furthermore, the C 1s peak centered at 284.4 eV (Fig. 3e) is ascribed to the presence of non-oxygenated sp^2 C in the basal plane of rGO, and the fitted peak observed at the higher binding energy reveals the presence of a trace amount of oxygen-containing functional groups in rGO.[40,41] This feature supports the aforementioned Raman result.

The HER measurement was made using the standard three electrode configuration in the 0.5 M H_2SO_4 electrolyte with Pt as a counter electrode, SCE as a reference electrode and the material under investigation as the working electrode. Linear sweep voltammetry was performed at a scan rate of 2 mV s^{-1}. During the measurement, the system was continuously deaerated with N_2 (see the Experimental section). In order to demonstrate the HER activity, the polarization curves were derived from the respective linear sweep voltammograms. In line with this, Fig. 4 shows the iR corrected polarization curves for WS_2 nanosheets and rGO/WS_2 nanosheets. It is observed that the overall HER efficiency improved in the case of rGO/WS_2 as compared to the naked WS_2. A current density of 10 mA cm^{-2} is achieved at 229 mV for rGO/WS_2 and at 236 mV for that of WS_2. This is still interesting so far as improvement is concerned as compared to the recently reported[3] value (270 mV) which employed WS_2/rGO on the glassy carbon electrode. This can be accounted for by the fact that the rGO on the surface of the vertically aligned WS_2 nanosheet tends to have more chance to contribute to the electron mobility than the other way round, *i.e.* the condition where the WS_2 nanosheets on the surface of rGO might limit the effect of graphene. For further insight into the electrocatalytic activity of the electrodes, the Tafel plots (Fig. 4b), as one of the key parameters for the viability of HER, were derived from the polarization curves. The linear parts of the Tafel plots were fitted to the Tafel equation ($\eta = b \log j + a$, where b is the Tafel slope and j is the current density) and the slopes were calculated to assess the kinetics of the charge transfer process. In this respect, the Tafel slope of rGO/WS_2 is smaller (73 mV dec^{-1}) as compared to WS_2 (97 mV dec^{-1}). This reveals that rGO/WS_2 possesses a faster kinetics of HER with increasing overpotential. The observed smaller over potential and Tafel slope exhibited by rGO/WS_2 can be attributed to the intimate contact between rGO and WS_2 that results in a conducive environment for facile electron transport. Another important criterion for a good electrocatalyst is its electrochemically active surface area. Estimation of electrochemical double layer capacitance (C_{dl}) is indicative of the electrochemically active surface area, and was made by running the cyclic voltammeter (CV) at various scan rates in the potential range of −0.1 to 0.0 V *vs.* RHE (Fig. S4†). Half the difference of the positive and negative current densities at the middle of the potential *vs.* the scan rate is plotted (Fig. 4c) to find out the slope which is C_{dl}. Accordingly, the enhanced electrochemical active area in rGO/WS_2 is demonstrated by increased C_{dl} (5.8 mF cm^{-2}) as compared to that of WS_2 (1.08 mF cm^{-2}). Furthermore, as can be seen from the Nyquist plot (Fig. 4d), the impedance of rGO/WS_2 is significantly lower than that of the bare WS_2. The charge transfer resistances (R_{ct}) are 31.6 Ω and 50.29 Ω for rGO/WS_2 and WS_2 nanosheets respectively. This shows the excellent conductivity bestowed by rGO to the surface of WS_2 nanosheets. Additionally, the small series resistance (0.98 Ω–1.29 Ω) reveals the importance of the conductive W foil substrate that integrates with the WS_2–rGO system thereby minimizing ohmic losses. The series resistance of rGO/WS_2 is also lower than that of the naked WS_2 nanosheets (the top inset of Fig. 4d). The equivalent electrical circuit, in the bottom inset of Fig. 4d, consists of a series resistance (R_s), a constant phase element (CPE), and a charge transfer resistance (R_{ct}) related to the HER process, modelling the EIS data. We attribute these facts to: (i) the exposed edges of vertically aligned WS_2 nanosheets, (ii) decoration by rGO through a remarkable area of contact that enhanced the electron transport phenomena and (iii) the conductive W foil substrate which plays its own role for facile electrode kinetics.

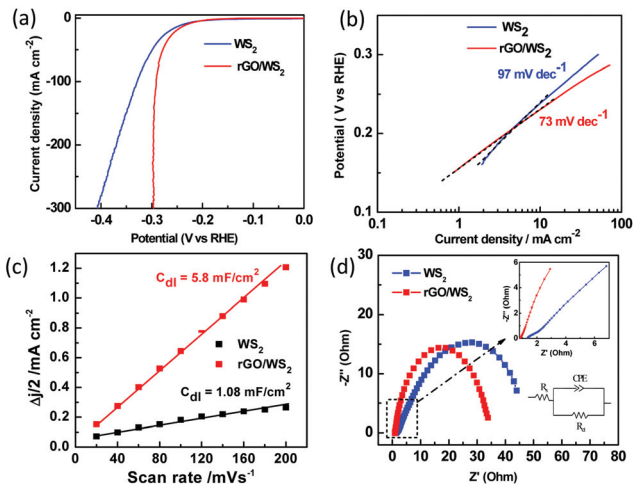

Fig. 4 HER measurements of WS_2 and rGO/WS_2, (a) polarization curve, (b) Tafel plots, (c) linear fitting made to estimate the electrochemical active surface area and (d) Nyquist plot.

Conclusions

In summary, we have successfully synthesized vertically aligned WS_2 nanosheets on a W foil substrate through a hydrothermal method followed by a sulfidation method. We have also developed a method through which the surface activity of WS_2 nanosheets can be enhanced by decoration with reduced graphene oxide. Due to the fact that each nanotree of the WO_3 morphology was composed of several branches that tend to

behave like nanosheets, the sulfurization process ends up in the nanosheet morphology. More importantly, the vertically positioned frame was maintained. The enhanced electrocatalytic activity brought about by the synergism of WS_2 nanosheets and rGO is demonstrated by the achievement of a considerable current density at a smaller potential, accompanied by a smaller Tafel slope in HER measurement. The self-seeded substrate, onto which the nanosheets grew, also took part in the betterment of the HER activity. We, therefore, believe that our achievement has brought about a tangible contribution in the area of electrocatalysis. Moreover, it will also open the door for applications of other optoelectronic devices.

Acknowledgements

This work at the National Center for Nanoscience and Technology was supported by the 973 Program of the Ministry of Science and Technology of China (no. 2012CB934103), the 100-Talents Program of the Chinese Academy of Sciences (no. Y1172911ZX), the National Natural Science Foundation of China (no. 21373065 and 61474033) and the Beijing Natural Science Foundation (no. 2144059).

Notes and references

1 D. Larcher and J. M. Tarascon, *Nat. Chem.*, 2015, **7**, 19–29.
2 J. A. Turner, *Science*, 2004, **305**, 972–974.
3 J. Yang, D. Voiry, S. J. Ahn, D. Kang, A. Y. Kim, M. Chhowalla and H. S. Shin, *Angew. Chem., Int. Ed.*, 2013, **52**, 13751–13754.
4 M. A. Lukowski, A. S. Daniel, C. R. English, F. Meng, A. Forticaux, R. J. Hamers and S. Jin, *Energy Environ. Sci.*, 2014, **7**, 2608.
5 D. Voiry, H. Yamaguchi, J. Li, R. Silva, D. C. B. Alves, T. Fujita, M. Chen, T. Asefa, V. B. Shenoy, G. Eda and M. Chhowalla, *Nat. Mater.*, 2013, **12**, 850–855.
6 M. S. Faber and S. Jin, *Energy Environ. Sci.*, 2014, **7**, 3519–3542.
7 D. Merki and X. Hu, *Energy Environ. Sci.*, 2011, **4**, 3878.
8 D. Y. Chung, S. K. Park, Y. H. Chung, S. H. Yu, D. H. Lim, N. Jung, H. C. Ham, H. Y. Park, Y. Piao, S. J. Yoo and Y. E. Sung, *Nanoscale*, 2014, **6**, 2131–2136.
9 Y. Shi, J. K. Huang, L. Jin, Y. T. Hsu, S. F. Yu, L. J. Li and H. Y. Yang, *Sci. Rep.*, 2013, **3**, 1839.
10 M. Chhowalla, H. S. Shin, G. Eda, L.-J. Li, K. P. Loh and H. Zhang, *Nat. Chem.*, 2013, **5**, 263–275.
11 K. Xu, F. Wang, Z. Wang, X. Zhan, Q. Wang, Z. Cheng, M. Safdar and J. He, *ACS Nano*, 2014, **8**, 8468–8476.
12 T. F. Jaramillo, K. P. Jørgensen, J. Bonde, J. H. Nielsen, S. Horch and I. Chorkendorff, *Science*, 2007, **317**, 100–102.
13 J. Kibsgaard, T. F. Jaramillo and F. Besenbacher, *Nat. Chem.*, 2014, **6**, 248–253.
14 M. A. Lukowski, A. S. Daniel, F. Meng, A. Forticaux, L. Li and S. Jin, *J. Am. Chem. Soc.*, 2013, **135**, 10274–10277.
15 N. Peimyoo, J. Shang, C. Cong, X. Shen, X. Wu, E. K. L. Yeow and T. Yu, *ACS Nano*, 2013, **7**, 10985–10994.
16 D. Ovchinnikov, A. Allain, Y.-S. Huang, D. Dumcenco and A. Kis, *ACS Nano*, 2014, **8**, 8174–8181.
17 M. Bernardi, M. Palummo and J. C. Grossman, *Nano Lett.*, 2013, **13**, 3664–3670.
18 X. Zong, J. Han, G. Ma, H. Yan, G. Wu and C. Li, *J. Phys. Chem. C*, 2011, **115**, 12202–12208.
19 Q. Mahmood, M. G. Kim, S. Yun, S. M. Bak, X. Q. Yang, H. S. Shin, W. S. Kim, P. V. Braun and H. S. Park, *Nano Lett.*, 2015, **15**, 2269–2277.
20 Z. Wu, B. Fang, A. Bonakdarpour, A. Sun, D. P. Wilkinson and D. Wang, *Appl. Catal., B*, 2012, **125**, 59–66.
21 Y. Yuan, R. Li and Z. Liu, *Anal. Chem.*, 2014, **86**, 3610–3615.
22 B. Mahler, V. Hoepfner, K. Liao and G. A. Ozin, *J. Am. Chem. Soc.*, 2014, **136**, 14121–14127.
23 Y. Zhang, Y. Zhang, Q. Ji, J. Ju, H. Yuan, J. Shi, T. Gao, D. Ma, M. Liu, Y. Chen, X. Song, H. Y. Hwang, Y. Cui and Z. Liu, *ACS Nano*, 2013, **7**, 8963–8971.
24 H. Wu, M. Xu, P. Da, W. Li, D. Jia and G. Zheng, *Phys. Chem. Chem. Phys.*, 2013, **15**, 16138–16142.
25 K. Kośmider and J. Fernández-Rossier, *Phys. Rev. B: Condens. Matter*, 2013, **87**, 075451.
26 L. Britnell, R. M. Ribeiro, A. Eckmann, R. Jalil, B. D. Belle, A. Mishchenko, Y.-J. Kim, R. V. Gorbachev, T. Georgiou, S. V. Morozov, A. N. Grigorenko, A. K. Geim, C. Casiraghi, A. H. C. Neto and K. S. Novoselov, *Science*, 2013, **340**, 1311–1314.
27 L. Liao, J. Zhu, X. Bian, L. Zhu, M. D. Scanlon, H. H. Girault and B. Liu, *Adv. Funct. Mater.*, 2013, **23**, 5326–5333.
28 D. J. Li, U. N. Maiti, J. Lim, D. S. Choi, W. J. Lee, Y. Oh, G. Y. Lee and S. O. Kim, *Nano Lett.*, 2014, **14**, 1228–1233.
29 B. Xia, Y. Yan, X. Wang and X. W. Lou, *Mater. Horiz.*, 2014, **1**, 379–399.
30 C. Tan and H. Zhang, *Chem. Soc. Rev.*, 2015, **44**, 2713.
31 S.-S. Li and C.-W. Zhang, *J. Appl. Phys.*, 2013, **114**, 183709.
32 F. Wang, Y. Li, Z. Cheng, K. Xu, X. Zhan, Z. Wang and J. He, *Phys. Chem. Chem. Phys.*, 2014, **16**, 12214–12220.
33 W. S. Hummers and R. E. Offeman, *J. Am. Chem. Soc.*, 1958, **80**, 1339–1339.
34 S. K. Bhunia and N. R. Jana, *ACS Appl. Mater. Interfaces*, 2014, **6**, 20085–20092.
35 A. Michailovski, R. Kiebach, W. Bensch, J.-D. Grunwaldt, A. Baiker, S. Komarneni and G. R. Patzke, *Chem. Mater.*, 2007, **19**, 185–197.
36 M. Shibuya and M. Miyauchi, *Adv. Mater.*, 2009, **21**, 1373–1376.
37 R. F. Garcia-Sanchez, T. Ahmido, D. Casimir, S. Baliga and P. Misra, *J. Phys. Chem. A*, 2013, **117**, 13825–13831.
38 A. Berkdemir, H. R. Gutiérrez, A. R. Botello-Méndez, N. Perea-López, A. L. Elías, C.-I. Chia, B. Wang,

V. H. Crespi, F. López-Urías, J.-C. Charlier, H. Terrones and M. Terrones, *Sci. Rep.*, 2013, 3.
39 D. O. Dumcenco, K. Y. Chen, Y. P. Wang, Y. S. Huang and K. K. Tiong, *J. Alloys Compd.*, 2010, **506**, 940–943.
40 C. S. Rout, B. H. Kim, X. Xu, J. Yang, H. Y. Jeong, D. Odkhuu, N. Park, J. Cho and H. S. Shin, *J. Am. Chem. Soc.*, 2013, **135**, 8720–8725.
41 S. Pei and H.-M. Cheng, *Carbon*, 2012, **50**, 3210–3228.